In-plane heterostructured MoN/Mo_2N nanosheets as high-efficiency electrocatalysts for alkaline hydrogen evolution reaction

Cite as: APL Mater. 11, 061118 (2023); doi: 10.1063/5.0150039
Submitted: 10 March 2023 • Accepted: 25 May 2023 •
Published Online: 12 June 2023

Xiuen Luo,[1,2] Hao Song,[1,3] Yulei Ren,[1] Xuming Zhang,[1] Kaifu Huo,[2,4,a)] and Paul K. Chu[3]

AFFILIATIONS

[1] The State Key Laboratory of Refractories and Metallurgy, Institute of Advanced Materials and Nanotechnology, Wuhan University of Science and Technology, Wuhan 430081, China
[2] Wuhan National Laboratory for Optoelectronics (WNLO), Huazhong University of Science and Technology, Wuhan 430074, China
[3] Department of Physics, Department of Materials Science and Engineering, and Department of Biomedical Engineering, City University of Hong Kong, Tat Chee Avenue, Hong Kong, China
[4] Research Institute of Huazhong University of Science and Technology in Shenzhen, Shenzhen 518063, China

Note: This paper is part of the Special Topic on Materials Challenges for Catalysis.
[a)] **Author to whom correspondence should be addressed:** kfhuo@hust.edu.cn

ABSTRACT

Economical and efficient electrocatalysts are crucial to the hydrogen evolution reaction (HER) in water splitting to produce hydrogen. Heterostructured electrocatalysts generally exhibit enhanced HER catalytic activity due to the strong electron coupling effects and synergistic optimization of hydrogen adsorption–desorption. Herein, in-plane heterostructured MoN/Mo_2N nanosheets are fabricated as high-efficiency HER electrocatalysts in the alkaline medium from bulk MoS_2 by molten salt-assisted synthesis. Density-functional theory calculations and experiments show that the in-plane heterostructured MoN/Mo_2N nanosheets facilitate interfacial electron redistribution from Mo_2N to MoN, giving rise to more negative H_2O adsorption energy and optimal hydrogen adsorption free energy (ΔG_{H^*} = −0.017 eV). Consequently, a low overpotential of 126 mV at 10 mA cm^{-2} and a small Tafel slope of 69.5 mV dec^{-1} are achieved in the 1M KOH electrolyte, demonstrating excellent HER characteristics. Moreover, the overpotential shows negligible change after operating at 50 mA cm^{-2} for 12 h, confirming the excellent stability. The results reveal a novel and effective strategy to design highly efficient 2D in-plane heterostructured HER electrocatalysts for water splitting.

I. INTRODUCTION

The hydrogen evolution reaction (HER) is an environmentally friendly and promising approach to produce clean hydrogen (H_2) via water splitting, and high-efficiency and durable electrocatalysts are crucial to reduce the overpotential and promote the HER efficiency.[1–3] Although platinum (Pt) shows excellent HER activity, their high cost and scarcity have hampered the use of industrial water splitting to produce hydrogen.[4,5] Therefore, it is essential to design and develop alternative non-precious metal-based HER catalysts. In recent years, transition metal compounds, such as metal phosphides,[6] carbides,[7] nitrides,[8] sulfides,[9] and borides,[10] have been investigated as alternative HER catalysts. In particular, molybdenum-based nitrides, such as MoN and Mo_2N, have garnered increasing attention due to their metal-like conductivity, good corrosion resistance, and favorable d-band electronic structure.

Two-dimensional (2D) molybdenum nitrides possess enhanced HER properties due to their unsaturated dangling bonds and abundant active sites.[11] However, single-phase 2D MoN or Mo_2N delivers unsatisfactory HER performance due to their lopsided hydrogen adsorption–desorption free energy. In this context, proper heterostructures can improve the HER catalytic activity by adjusting the local electronic structure at the interface, optimizing the water dissociation capability, and balancing hydrogen

adsorption–desorption. For example, in the work of Sun *et al.*, the authors have reported an Co/MoN heterogeneous nanoflake array with enhanced water dissociation capability in alkaline HER process as a result of promoted electron transport from Co to MoN.[12] In the work of Lin *et al.*, a MoN–MnO heterostructure nanosheet catalyst with the interfacial-O configuration has been described, which enables fast hydrogen coupling and desorption on the nitride domains leading to enhanced HER activity in alkaline media.[13] However, preparation of MoN nanosheets is usually complicated and the second phases are generally deposited on the MoN surface, resulting in limited active sites. In this context, construction of 2D in-plane nitride heterojunctions with strong electron coupling may deliver better HER performance by taking advantage of the more abundant active sites and better balance between adsorption and desorption of hydrogen. However, controllable and facile synthesis of the 2D heterostructured MoN/Mo_2N nanosheets with robust heterointerfaces is still challenging.

Herein, a flower-like 2D heterostructured MoN/Mo_2N nanosheets electrocatalyst is designed and demonstrated to be high-efficiency alkaline HER catalysts. The 2D MoN/Mo_2N nanosheets are synthesized from bulk MoS_2 by Na_2CO_3-assisted thermal nitriding under NH_3 and subsequent annealing in Ar/H_2 as schematically illustrated in Fig. 1(a). The flower-like 2D heterostructured MoN/Mo_2N nanosheets have several advantages in HER. First, the 2D MoN/Mo_2N hybrid structure provides abundant active sites and robust heterointerfaces which facilitate access of electrolytes and release of H_2 bubbles due to the 2D structure and flower-like morphology. Second, the 2D in-plane MoN/Mo_2N interfaces optimize H adsorption/desorption by coupling strong hydrogen adsorption of MoN and weak hydrogen adsorption of Mo_2N, consequently yielding an optimal hydrogen adsorption free energy for MoN/Mo_2N (ΔG_{H^*} = −0.017 eV). Third, the ratio of MoN/Mo_2N can be optimized by controlling the annealing temperature and time in the Ar/H_2 ambient. The optimal in-plane MoN/Mo_2N heterostructured nanosheets exhibit excellent HER activity as exemplified by a low overpotential of 126 mV at 10 mA cm^{-2} and a small Tafel slope of 69.5 mV dec^{-1} in alkaline media, which are superior to those of recently reported MoN- and Mo_2N-based electrocatalysts (Table S1).[14–22] Moreover, the 2D MoN/Mo_2N nanosheets exhibit remarkable stability with only negligible potential changes at a high current density of 50 mA cm^{-2} after 12 h. The results demonstrate a novel strategy to construct 2D in-plane heterostructured TMNs catalysts for high-performance electrocatalytic water splitting.

II. EXPERIMENTAL SECTION

A. Chemicals and materials

All the chemicals were used without further purification. Molybdenum disulfide (MoS_2, 99.5%) was purchased from Aladdin and sodium carbonate (Na_2CO_3, ≥99.8%) and hydrochloric acid (HCl, 36%–38.0%) were purchased from Sinopharm Chemical Reagent Co, Ltd.

B. Synthesis of 2D MoN/Mo_2N nanosheets

The MoN nanosheets were prepared from the bulk MoS_2 precursor by Na_2CO_3-assisted salt synthesis.[23] In the typical synthesis, the MoS_2 and Na_2CO_3 powders with a molar ratio of 1:2.5 were mixed in a mortar and annealed in a quartz tube furnace at 750 °C with a heating rate of 10 °C/min for 3 h under NH_3. After cooling to room temperature, the product was collected, washed with 1M HCl for 2 h, and rinsed with de-ionized water several times.

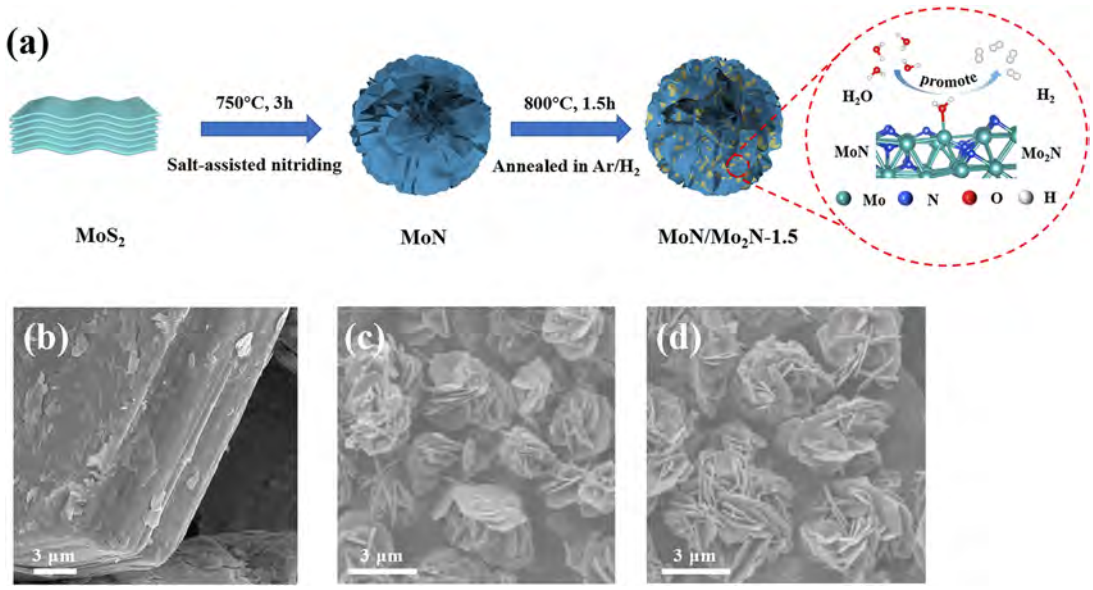

FIG. 1. Preparation process. (a) Schematic illustration of the preparation of MoN/Mo_2N; SEM images of (b) MoS_2, (c) MoN, and (d) MoN/Mo_2N-1.5.

The MoN nanosheet powder was obtained after freeze drying. The MoN nanosheets were then annealed under Ar/H_2 to produce the MoN/Mo_2N heterojunction nanosheets at 800 °C with a heating rate of 10 °C/min. The ratio of MoN/Mo_2N was controlled via adjusting the annealing time (1.0, 1.5, and 3.0 h and samples denoted as MoN/Mo_2N-1, MoN/Mo_2N-1.5, and MoN/Mo_2N-3). The Mo_2N nanosheets were obtained by further annealing MoN/Mo_2N-1.5 nanosheets at 800 °C for 8 h under Ar/H_2.

C. Characterization and electrochemical assessment

1. Materials characterization

The morphology and microstructure of the materials were characterized by field-emission scanning electron microscopy (FE-SEM, ThermoFisher/Apreo S HiVac) and transmission electron microscopy (TEM, JEM-F200). The crystal structure was analyzed by x-ray diffraction (XRD, Rigaku/SmartLab) and elemental maps were acquired by energy-dispersive x-ray spectroscopy (EDS, OXFORD AZtecLive Ultim Max 100). The chemical states were determined by x-ray photoelectron spectroscopy (XPS, ESCALab250).

2. Electrochemical measurements

The electrochemical measurements were carried out in 1.0M KOH electrolyte using a three-electrode system on electrochemical workstation (Bio-logical VMP 300). To prepare the working electrode, 6 mg of the sample, 20 μl of Nafion, 100 μl of de-ionized water, and 900 μl of isopropanol were mixed, sonicated for 40 min, and introduced onto a copper foam dropwise. The copper foam was heated in an oven at 70 °C for 10 min and 40 μl of diluted tenfold Nafion was used as the protective layer. The modified copper foam electrode was dried at 25 °C in air for 18 h. In the three-electrode system, the electrocatalyst-loaded copper foam ($1 \times 1.2 \times 0.1$ cm^3) was the working electrode, graphite rod was the counter-electrode, and saturated calomel electrode (SCE) was the reference electrode. All the potentials were iR corrected and calibrated with reference to the reversible hydrogen electrode (RHE) according to Nernst equation ($E_{RHE} = E_{SCE} + 0.241 + 0.0592 \times pH$). The activity of the working electrode was evaluated by linear sweep voltammetry (LSV) at 5 mV s^{-1}. Electrochemical impedance spectroscopy (EIS) was conducted between 100 kHz and 0.01 Hz with an AC perturbation of 5 mV and the electric double-layer capacitance was obtained via cyclic voltammetry (CV) from 10 to 60 mV s^{-1} in the non-Faradic region between −0.72 and −0.82 V vs SCE. To evaluate the electrochemical stability of MoN/Mo_2N, CV was carried out for 5000 cycles at a scanning rate of 100 mV s^{-1} and a galvanostatic test was conducted at a current density of 50 mA cm^{-2}, and the LSV curves before and after cycling at 5 mV s^{-1} were recorded.

3. Theoretical calculation

The density-functional theory (DFT) calculation was carried out using the (200) plane of MoN and (111) plane of Mo_2N based on the XRD and HR-TEM results. The *Vienna Ab initio* Simulation Package (VASP) was employed in the density-functional theory (DFT) calculation adopting the generalized gradient approximation (GGA) with the Perdew–Burke–Ernzerhof (PBE) functional.[24,25] The projected augmented wave (PAW) potentials were chosen to describe the ionic cores and valence electrons were taken into account using the plane wave basis set with a kinetic energy cutoff of 400 eV. The implicit solvation model implemented in VASPsol was used to calculate E_{sol} and the DFT-D3 empirical correction method was employed to describe the van der Waals interactions. Geometric optimization was conducted with the force convergence smaller than 0.05 eV/Å and the Monkhorst–Pack k-points of $2 \times 2 \times 1$, $2 \times 2 \times 1$, and $1 \times 2 \times 1$ were applied to Mo_2N (111), MoN (200), and MoN/Mo_2N, respectively. The atoms on the bottom were fixed in the calculation. The adsorption energy (E_a) was calculated by the equation

$$E_a = E_{(slab+H_2O)} - E_{(slab)} - E_{(H_2O)},$$

where $E_{(slab+H_2O)}$ and $E_{(slab)}$ are the total energy of the surface slab with and without H_2O adsorption, respectively, and $E_{(H_2O)}$ is the total energy of the H_2O molecule in the gas phase. The hydrogen adsorption energy (ΔE_{H^*}) was calculated by the equation

$$\Delta E_{H*} = E_{H*} - E_{(H/slab)} - 1/2E_{(H_2)},$$

where E_{H^*} and $E_{(H/slab)}$ are the total energy of the surface slab with and without atomic H adsorption, respectively. $E_{(H_2)}$ is the total energy of the H_2 molecule in the gas phase. Moreover, the Gibbs free energy change in the discharging step in HER under standard conditions was approximated as $\Delta G_{H^*} = \Delta E_{H^*} + 0.2$ eV.[26,27]

III. RESULTS AND DISCUSSION

The 2D in-plane heterostructured $MoN–Mo_2N$ nanosheets are prepared by two steps [Fig. 1(a)]. The flower-like MoN assembled by 2D nanosheets is prepared from bulk MoS_2 by Na_2CO_3-assisted thermal nitriding under NH_3 at 750 °C for 3 h.[23] The bulk MoS_2 precursor with a layered structure has an average size of 50 μm and thickness of 10 μm [Figs. 1(b) and S1(a)]. The sharp (002) diffraction peak observed from bulk MoS_2 (PDF# 37–1492) [Fig. S1(b)] discloses high crystallinity.[28] After Na_2CO_3-assisted thermal nitriding reaction, the layered MoS_2 power is fully converted into flower-like morphology assembled by 2D nanosheets with a thickness of 6.2 nm [Figs. 1(c) and S2]. XRD patterns of the product is ascribed to hexagonal MoN (PDF# 25–1367) and no MoS_2 peaks are observed, suggesting that the MoS_2 is fully converted into 2D MoN nanosheets. The 2D heterostructured MoN/Mo_2N nanosheets are prepared by further annealing the MoN nanosheets under Ar/H_2. The MoN/Mo_2N structure retains a similar flower-like morphology with an average particle size of 5 μm [Fig. 1(d)].

The XRD patterns of MoN/Mo_2N-1, MoN/Mo_2N-1.5, and MoN/Mo_2N-3 are depicted in Fig. S3. The characteristic peaks at 37.4°, 43.5°, 63.2°, and 75.7° correspond to the (111), (200), (220), and (311) facets of cubic Mo_2N (PDF# 25–1366) [Fig. 2(a)]. Moreover, the amount of Mo_2N in the MoN/Mo_2N nanosheets increases with annealing time (Fig. S3). After further annealing MoN/Mo_2N for 8 h under Ar/H_2, only Mo_2N phase is observed, suggesting formation of single-phase Mo_2N nanosheets [Fig. 2(a)]. The MoN, MoN/Mo_2N, and Mo_2N have the similar morphology, suggesting topochemical chemical conversion from MoN to MoN/Mo_2N and Mo_2N (Fig. S4). The chemical states of MoN/Mo_2N-1.5 are determined by XPS. XPS full-scan survey reveals the existence of Mo and N elements in MoN/Mo_2N-1.5 [Fig. S5(a)]. High-resolution Mo 3*d* XPS spectra can be resolved to four pairs of $3d_{5/2}/3d_{3/2}$

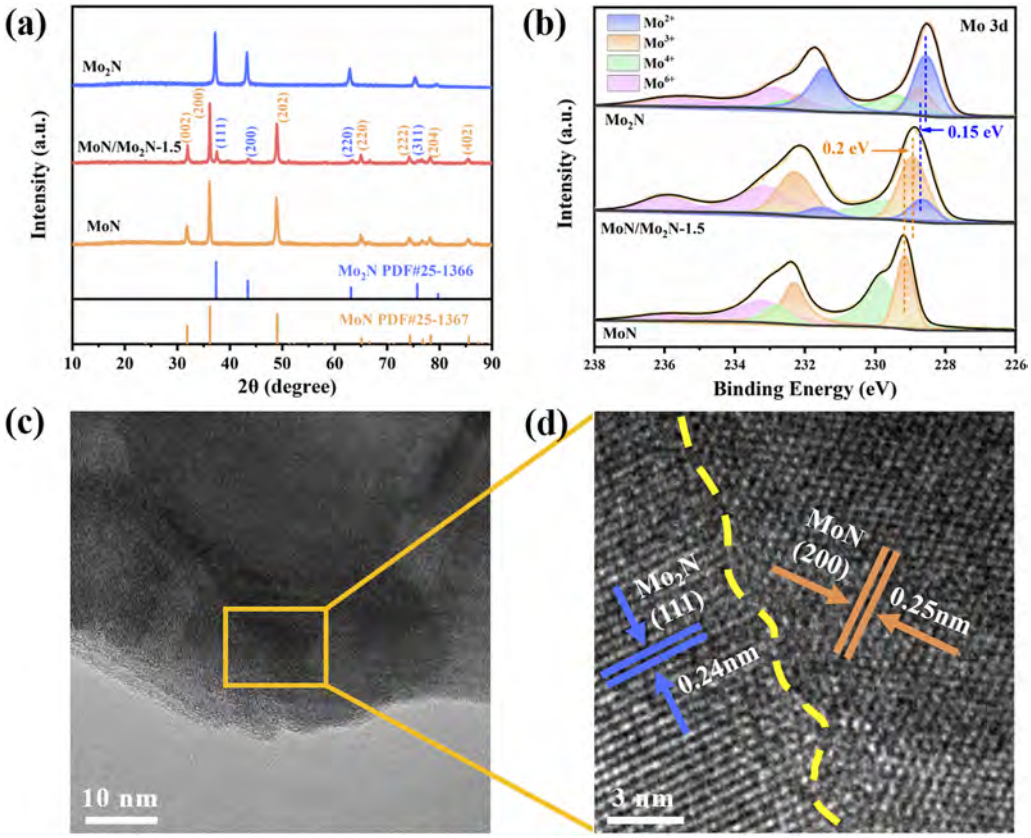

FIG. 2. Structure and morphology. (a) XRD patterns of MoN, MoN/Mo_2N-1.5, and Mo_2N; (b) XPS Mo 3*d* spectra of MoN (bottom), MoN/Mo_2N-1.5 (middle), and Mo_2N (top); (c)–(d) TEM and HR-TEM images of MoN/Mo_2N-1.5, revealing distinct interfaces between MoN and Mo_2N phases.

doublets: for Mo^{2+} (228.7/231.8 eV), Mo^{3+} (228.9/232.1 eV), Mo^{4+} (229.7/232.6 eV), Mo^{6+} (233.1/235.9 eV) [Fig. 2(b)].[29–32] It has been suggested the dominance of Mo^{2+} in Mo_2N and Mo^{3+} in MoN and higher valence states of Mo^{4+} and Mo^{6+} are due to partial surface oxidation.[33–35] Notably, the Mo^{3+} peak red shifts (~0.2 eV), whereas the Mo^{2+} peak blue shifts (~0.15 eV), suggesting electron transfer from Mo_2N to MoN in MoN/Mo_2N. The N 1 *s* spectrum of MoN/Mo_2N-1.5 in Fig. S5(b) shows two deconvoluted peaks at 397.9, and 399.3 eV attributing to Mo–N bond, and N–H bond, respectively.[36–40] Similarly, there are two O 1 *s* peaks [Fig. S5(c)] at 530.9 and 532.1 eV arising from N–Mo-O_x and N–Mo-$(OH)_x$ in MoN/Mo_2N due to surface oxidation during XPS test.[33–35,41,42]

TEM and HR-TEM images are depicted in Figs. 2(c) and 2(d). Distinct interfaces between MoN and Mo_2N phases are observed. The (200) crystal plane of MoN forms an interface with the (111) crystal plane of Mo_2N with interplanar distances of ~0.25 and ~0.24 nm, respectively.[43] To further investigate the formation process of the in-plane MoN/Mo_2N heterojunctions, MoN/Mo_2N-3 with a higher Mo_2N concentration is immersed in 6M NaOH solution at 80 °C for 5 min and the composition and structure before and after immersion are evaluated by XRD and TEM. After alkali washing, the intensity of the XRD peaks of Mo_2N of MoN/Mo_2N-3 (Fig. S6) decreases, indicating that the Mo_2N phase has been partially removed during this alkali etching process. The TEM images of MoN/Mo_2N-3 after alkali immersion (Fig. S7) show a large number of pores formed as a result of washing away Mo_2N. Hence, it is conjectured that the MoN phase is partially reduced to form Mo_2N by annealing MoN under Ar/H_2, resulting in the formation of in-plane MoN/Mo_2N heterojunction interface (Fig. S8). The elemental maps (Fig. S9) reveal homogeneous distributions of Mo and N in the MoN/Mo_2N nanosheets.

The HER electrocatalytic characteristics of MoN, MoN/Mo_2N, and Mo_2N samples are evaluated in 1M KOH electrolyte. The electrocatalysts are drop-coated on the copper foam that has negligible HER activity. The commercial 20 wt. % Pt/C with the same mass loading dispersed on copper foam is also studied for comparison.[44] As shown in Fig. 3(a), the in-plane heterostructured MoN/Mo_2N electrode shows enhanced HER activity compared with MoN and Mo_2N nanosheets. To reach current densities of 10 and 100 mA cm^{-2}, MoN/Mo_2N-1.5 only requires low overpotentials of 126 and 220 mV, respectively, which are lower than those of MoN (249 and 360 mV), Mo_2N (221 and 344 mV) and the other Mo-based catalysts [Figs. 3(a) and S10, Table S1]. Figure 3(b) shows that the Tafel slope of MoN/Mo_2N-1.5 is 69.5 mV dec^{-1} and smaller than those of the MoN nanosheets (98.0 mV dec^{-1}) and Mo_2N (81.3 mV dec^{-1}), suggesting the Volmer–Heyrovsky mechanism.[45] The EIS results in

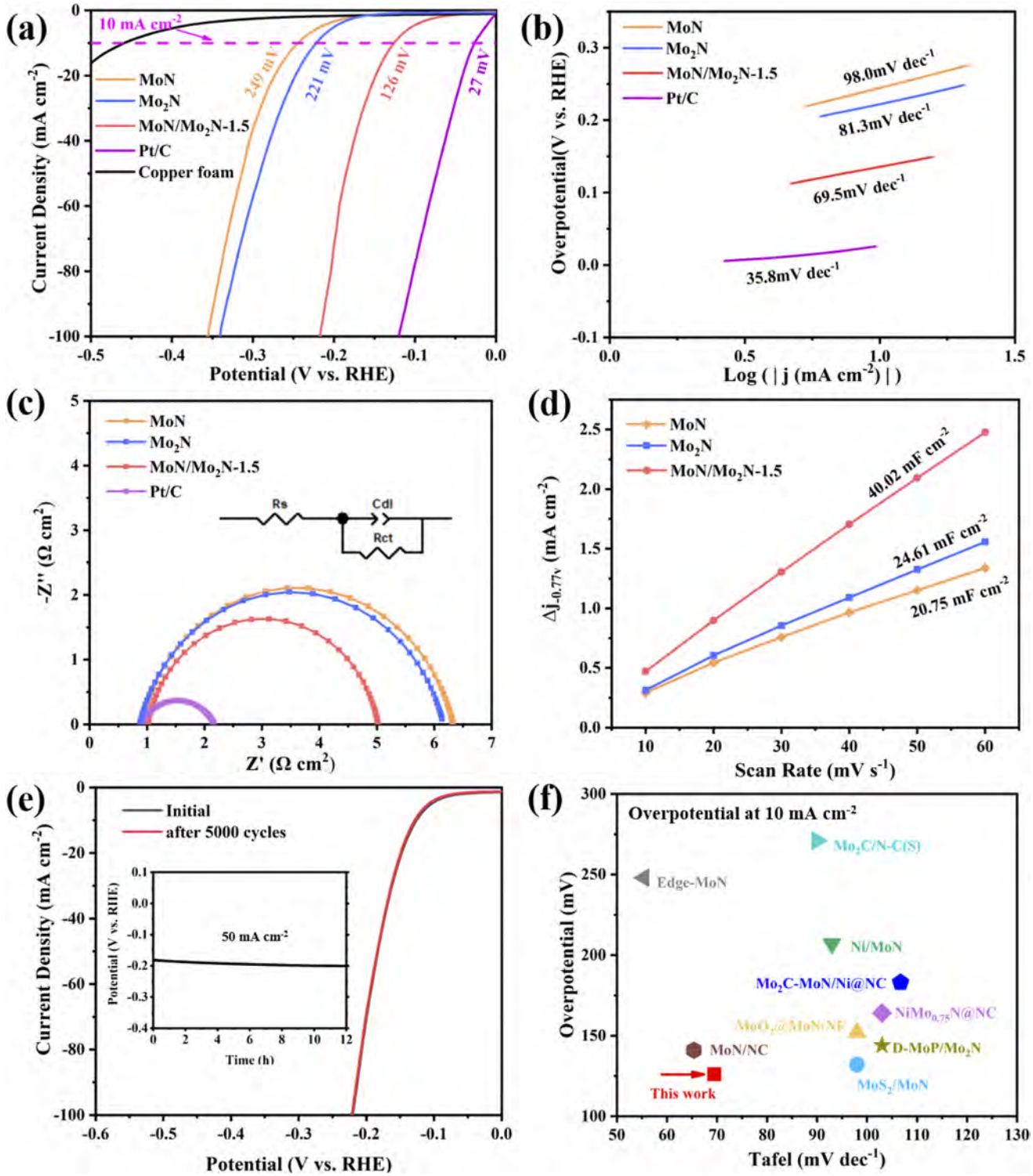

FIG. 3. HER activity in 1M KOH. (a) Polarization curves (LSV) of MoN, MoN/Mo_2N-1.5, Mo_2N, Pt/C, and Copper foam. (b)–(c) Tafel slopes and EIS curves of MoN, MoN/Mo_2N-1.5, Mo_2N, and Pt/C. (d) Double-layer capacitance (C_{dl}) plots of MoN, MoN/Mo_2N-1.5, and Mo_2N. (e) Polarization curves (LSV) of MoN/Mo_2N-1.5 before and after 5000 cycles (Inset: Stability of MoN/Mo_2N-1.5 at a current density of 50 mA cm^{-2}. (f) Comparison of overpotentials and Tafel slopes with other molybdenum-based nitride catalysts at 10 mA cm^{-2}.

Fig. 3(c) show that the charge transfer resistance of MoN/Mo_2N-1.5 is 4.0 Ω and smaller than those of MoN (5.4 Ω) and Mo_2N (5.2 Ω), indicative of fast interfacial charge transfer kinetics.[46] The electrochemical active surface area (ECSA) of MoN, MoN/Mo_2N-1.5, and Mo_2N is calculated by double-layer capacitance (C_{dl}) measurement experiments (Fig. S11). As shown in Fig. 3(d), the C_{dl} value of MoN/Mo_2N-1.5 is 40.02 mF cm^{-2}, which is larger than those of MoN (20.75 mF cm^{-2}) and Mo_2N (24.61 mF cm^{-2}), suggesting that MoN/Mo_2N-1.5 has more active sites. Since MoN, Mo_2N, and MoN/Mo_2N-1.5 have similar morphology, the morphology effect on HER activity is negligible. The intrinsic activities of MoN, Mo_2N, and MoN/Mo_2N-1.5 are analyzed by ECSA normalization (Fig. S12) and MoN/Mo_2N-1.5 shows the highest catalytic activity for HER. Continuous CV and chronopotentiometry tests are conducted to assess the stability of the MoN/Mo_2N-1.5 catalyst. As shown in Fig. 3(e), the polarization curves of MoN/Mo_2N-1.5 almost overlap with the initial one after 5000 CV cycles and the overpotentials show negligible change for 12 h at 50 mA cm^{-2}. SEM images reveal the flower-like morphology assembled by nanosheets are well-retained and XRD patterns have no change (Fig. S13). Moreover, the overpotential shows negligible change after operating at 50 mA cm^{-2} for 12 h, demonstrating good electrochemical stability of MoN/Mo_2N-1.5 in the alkaline electrolyte [Fig. 3(e)]. Figure 3(f) and Table. S1 compare the HER performance of MoN/Mo_2N-1.5 with other reported molybdenum-based nitride electrocatalysts, revealing MoN/Mo_2N-1.5 has excellent HER characteristics.[14–22]

To elucidate the mechanism of enhanced HER performance of the in-plane of MoN/Mo_2N, density-functional theory (DFT) calculation is carried out on the (200) plane of MoN and (111) plane of Mo_2N. Figures S14 and 4(a) show the geometric structures and charge density difference map of the MoN/Mo_2N heterojunction and the cyan and yellow regions in the charge density difference map represent loss and aggregation, respectively. The electron density of Mo_2N at the MoN/Mo_2N interface decreases and charges

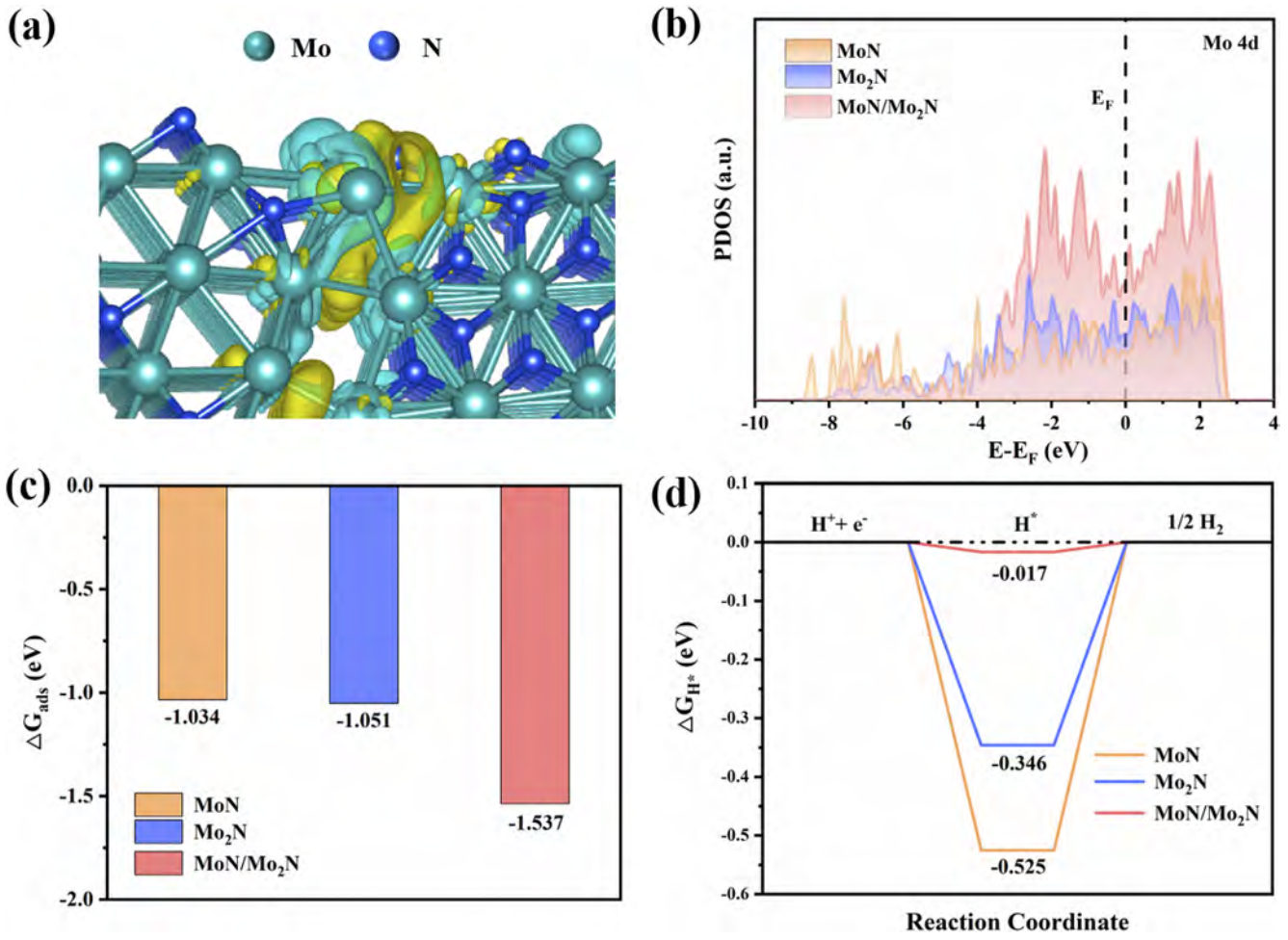

FIG. 4. Density-functional theory (DFT) calculation. (a) Charge density difference map of the MoN/Mo_2N heterojunction (cyan and yellow representing loss and aggregation of electrons, respectively). (b) Density of states (DOS) calculated on MoN, Mo_2N, and MoN/Mo_2N heterojunction. (c) and (d) Water adsorption energy and hydrogen adsorption free energy of MoN, Mo_2N, and MoN/Mo_2N.

aggregate at the Mo site of adjacent MoN in line with the XPS results. The density of state (DOS) of the Mo atoms on MoN, Mo_2N, and MoN/Mo_2N is calculated to analyze the interactions between the adsorbate and metal sites.[47] As shown in Fig. 4(b), the MoN/Mo_2N heterojunction has higher DOS than MoN and Mo_2N near the Fermi level (E_F) at the Mo site, indicating that electron rearrangement at the MoN/Mo_2N interface and more electrons on the Mo site promote H_2O adsorption and optimize H adsorption and desorption.[48,49] Based on the water adsorption model in Fig. S15, the calculated H_2O adsorption energy of the MoN/Mo_2N interface is −1.537 eV, which is less than that of MoN (−1.034 eV) and Mo_2N (−1.051 eV), indicating stronger adsorption capacity of water at the heterogeneous interface [Fig. 4(c)]. The hydrogen adsorption free energy (ΔG_{H^*}) is an important parameter for the HER activity and the closer ΔG_{H^*} is to zero, the more suitable the production of H_2.[50,51] Figures. 4(d) and S16 show the ΔG_{H^*} values of MoN, Mo_2N, and MoN/Mo_2N. ΔG_{H^*} of the Mo site at the interface of MoN (200)/Mo_2N (111) is −0.017 eV, which is lower than those of the Mo site on MoN (−0.525 eV) and Mo site on Mo_2N (−0.346 eV). These results suggest excellent HER activity on the heterogeneous MoN/Mo_2N catalyst in the alkaline solution, which is more conducive to water adsorption and hydrogen desorption, consequently boosting the enhanced HER activity and kinetics.

IV. CONCLUSION

In-plane heterostructured MoN/Mo_2N nanosheets are designed and demonstrated to be high-performance HER electrocatalysts in the alkaline medium. The in-plane heterostructured MoN/Mo_2N nanosheets exhibit a low overpotential of 126 mV at a current density of 10 mA cm^{-2} and a small Tafel slope of 69.5 mV dec^{-1} in the 1M KOH electrolyte, which are superior to those of recently reported Mo-based nitride electrocatalysts. DFT calculations and experiments show that electron transfer in the 2D in-plane interface between MoN and Mo_2N produces a more negative H_2O adsorption energy and moderate hydrogen adsorption free energy (ΔG_{H^*} = −0.017 eV). Moreover, the flower-like morphology of MoN/Mo_2N facilitates access of electrolytes and release of H_2 bubbles and the unique 2D structure increases exposure of active sites. This work is expected to pave a new way for new and rational design of highly efficient 2D in-plane heterostructured electrocatalysts for HER.

SUPPLEMENTARY MATERIAL

See the supplementary material for detailed experimental information and structural characterization [Figs. S1–S9 and S13], electrochemical performance tests [Figs. S10–S12], the atomic models of computation [Figs. S14–S16], and comparison table of electrochemical performance (Table S1).

ACKNOWLEDGMENTS

This work was financially supported by National Natural Science Foundation of China (Grant Nos. U2004210, 21875080, 51572100, and 52002297), the Basic Research Program of Shenzhen Municipal Science and Technology Innovation Committee (Grant No. JCYJ20210324141613032), Application Foundation Frontier Project of Wuhan Science and Technology (Grant No. 2020010601012199), Hubei Province Natural Science Foundation Innovation Group Project (Grant No. 2019CFA020), City University of Hong Kong Strategic Research Grant (SRG), Hong Kong, China (Grant No. 7005505), and City University of Hong Kong Donation Research Grant, Hong Kong, China (Grant No. DON-RMG 9229021). The authors are grateful to the facility support provided by the Analytical and Testing Center of HUST.

AUTHOR DECLARATIONS

Conflict of Interest

The authors have no conflicts to disclose.

Author Contributions

X.L. and H.S. contributed equally to this work.

Xiuen Luo: Formal analysis (equal); Investigation (equal); Validation (equal); Writing – original draft (equal). **Hao Song**: Formal analysis (equal); Investigation (equal); Validation (equal); Writing – original draft (equal). **Yulei Ren**: Data curation (equal); Investigation (equal). **Xuming Zhang**: Resources (equal); Writing – review & editing (equal). **Kaifu Huo**: Conceptualization (lead); Funding acquisition (lead); Project administration (equal); Supervision (lead); Writing – review & editing (lead). **Paul K. Chu**: Formal analysis (equal); Writing – review & editing (equal).

DATA AVAILABILITY

The data that support the findings of this study are available within the article and its supplementary material.

REFERENCES

[1] M. A. Rosen and S. Koohi-Fayegh, Energy, Energy Ecol. Environ. **1**, 10–29 (2016).
[2] F. Zhang, P. Zhao, M. Niu, and J. Maddy, Int. J. Hydrog. Energy **41**, 14535–14552 (2016).
[3] I. Staffell, D. Scamman, A. Velazquez Abad, P. Balcombe, P. E. Dodds, P. Ekins, N. Shah, and K. R. Ward, Energy Environ. Sci. **12**, 463–491 (2019).
[4] C. Jian, W. Hong, Q. Cai, J. Li, and W. Liu, Appl. Catal. B **266**, 118649 (2020).
[5] J. Kibsgaard and I. Chorkendorff, Nat. Energy **4**, 430–433 (2019).
[6] Q. Yue, Y. Wan, Z. Sun, X. Wu, Y. Yuan, and P. Du, J. Mater. Chem. A **3**, 16941–16947 (2015).
[7] L. Lin, W. Zhou, R. Gao, S. Yao, X. Zhang, W. Xu, S. Zheng, Z. Jiang, Q. Yu, and Y.-W. Li, Nature **544**, 80–83 (2017).
[8] C. Pi, X. Li, X. Zhang, H. Song, Y. Zheng, B. Gao, A. Kızılaslan, P. K. Chu, and K. Huo, Small **18**, 2201137 (2022).
[9] H. Wang, X. Xiao, S. Liu, C.-L. Chiang, X. Kuai, C.-K. Peng, Y.-C. Lin, X. Meng, J. Zhao, and J. Choi, J. Am. Chem. Soc. **141**, 18578–18584 (2019).
[10] P. R. Jothi, Y. Zhang, J. P. Scheifers, H. Park, and B. P. T. Fokwa, Sustainable Energy Fuels **1**, 1928–1934 (2017).
[11] Y. Wang, Z. Zhang, Y. Mao, and X. Wang, Energy Environ. Sci. **13**, 3993–4016 (2020).
[12] J. Sun, W. Xu, C. Lv, L. Zhang, M. Shakouri, Y. Peng, Q. Wang, X. Yang, D. Yuan, and M. Huang, Appl. Catal. B **286**, 119882 (2021).

[13]F. Lin, H. Qin, T. Wang, L. Yang, X. Cao, and L. Jiao, J. Mater. Chem. A **9**, 8325–8331 (2021).
[14]A. Wu, Y. Gu, Y. Xie, H. Yan, Y. Jiao, D. Wang, and C. Tian, J. Alloys Compd. **867**, 159066 (2021).
[15]Y. Sun, Y. Zhou, Y. Zhu, Y. Shen, and A. Xie, ACS Sustainable Chem. Eng. **7**, 9153–9163 (2019).
[16]B. Jiang, Y. Cui, S. Shi, N. Jiang, and W. Tan, Acta Chim. Sin. **80**, 1394 (2022).
[17]P. Wang, J. Qi, C. Li, X. Chen, T. Wang, and C. Liang, ChemElectroChem **7**, 745–752 (2020).
[18]Y. Wang, C. Jian, W. Hong, and W. Liu, Chem. Commun. **57**, 223–226 (2021).
[19]C. Huang, X.-L. Zhang, J. Tang, D. Li, Q.-D. Ruan, L.-L. Liu, F.-Y. Xiong, B. Wang, Y. Xu, S.-H. Cui, Y. Luo, Q.-W. Li, and P. K. Chu, Rare Metals **42**, 1446–1452 (2023).
[20]Y. Gu, A. Wu, Y. Jiao, H. Zheng, X. Wang, Y. Xie, L. Wang, C. Tian, and H. Fu, Angew. Chem. Int. Ed. **60**, 6673–6681 (2021).
[21]Y. Zhan, F. Xie, H. Zhang, Z. Lin, J. Huang, W. Zhang, X. Sun, H. Meng, Y. Zhang, and J. Chen, J. Electrochem. Soc. **165**, F75 (2018).
[22]M. Ji, S. Niu, Y. Du, B. Song, and P. Xu, ACS Sustainable Chem. Eng. **6**, 11922–11929 (2018).
[23]D. Gao, S. Deng, X. Li, Y. Zhang, T. Lv, Y. He, W. Mao, H. Yang, J. Zhang, and P. K. Chu, Chem. Eng. J. **454**, 140144 (2023).
[24]J. P. Perdew, K. Burke, and Y. Wang, Phys. Rev. B **54**, 016533 (1996).
[25]G. Kresse and D. Joubert, Phys. Rev. B **59**, 1758 (1999).
[26]Y. H. Li, P. F. Liu, L. F. Pan, H. F. Wang, Z. Z. Yang, L. R. Zheng, P. Hu, H. J. Zhao, L. Gu, and H. G. Yang, Nat. Commun. **6**, 8064 (2015).
[27]J. Yang, X. Chen, X. Liu, Y. Cao, J. Huang, Y. Li, and F. Liu, ACS Sustainable Chem. Eng. **9**, 5642–5650 (2021).
[28]N. Liu, P. Kim, J. H. Kim, J. H. Ye, S. Kim, and C. J. Lee, ACS Nano **8**, 6902–6910 (2014).
[29]Z. Wu, K. Yu, T. Guo, Z. Mu, D. Wang, and F. Liu, Electrochim. Acta **364**, 137219 (2020).
[30]H. Yan, Y. Xie, Y. Jiao, A. Wu, C. Tian, X. Zhang, L. Wang, and H. Fu, Adv. Mater. **30**, 1704156 (2018).
[31]C. Li, Z. Wang, M. Liu, E. Wang, B. Wang, L. Xu, K. Jiang, S. Fan, Y. Sun, and J. Li, Nat. Commun. **13**, 3338 (2022).
[32]J. Wang, W. Chen, T. Wang, N. Bate, C. Wang, and E. Wang, Nano Res. **11**, 4535–4548 (2018).
[33]D. O. Scanlon, G. W. Watson, D. J. Payne, G. R. Atkinson, R. G. Egdell, and D. S. L. Law, J. Phys. Chem. C **114**, 4636–4645 (2010).
[34]R. D. Nikam, A.-Y. Lu, P. A. Sonawane, U. R. Kumar, K. Yadav, L.-J. Li, and Y.-T. Chen, ACS Appl. Mater. Interfaces **7**, 23328–23335 (2015).
[35]D. Lee, Y. Kim, H. W. Kim, M. Choi, N. Park, H. Chang, Y. Kwon, J. H. Park, and H. J. Kim, J. Catal. **381**, 1–13 (2020).
[36]X. Xiao, H. Yu, H. Jin, M. Wu, Y. Fang, J. Sun, Z. Hu, T. Li, J. Wu, and L. Huang, ACS Nano **11**, 2180–2186 (2017).
[37]S. Xi, G. Lin, L. Jin, H. Li, and K. Xie, Nat. Commun. **10**, 4727 (2019).
[38]W. Liu, L. Yu, R. Yin, X. Xu, J. Feng, X. Jiang, D. Zheng, X. Gao, X. Gao, and W. Que, Small **16**, 1906775 (2020).
[39]S. Li, C. Cheng, A. Sagaltchik, P. Pachfule, C. Zhao, and A. Thomas, Adv. Funct. Mater. **29**, 1807419 (2019).
[40]L. Yu, Q. Zhu, S. Song, B. McElhenny, D. Wang, C. Wu, Z. Qin, J. Bao, Y. Yu, and S. Chen, Nat. Commun. **10**, 5106 (2019).
[41]P. Urbankowski, B. Anasori, K. Hantanasirisakul, L. Yang, L. Zhang, B. Haines, S. J. May, S. J. L. Billinge, and Y. Gogotsi, Nanoscale **9**, 17722–17730 (2017).
[42]B. Chen, M. Humayun, Y. Li, H. Zhang, H. Sun, Y. Wu, and C. Wang, ACS Sustainable Chem. Eng. **9**, 14180–14192 (2021).
[43]S. Dong, Y. S. Li, Z. L. Zhao, R. C. Li, J. Q. He, J. P. Yin, B. Yan, and X. Zhang, ChemistrySelect **7**, e202104041 (2022).
[44]M. Qiang, X. Zhang, H. Song, C. Pi, X. Wang, B. Gao, Y. Zheng, X. Peng, P. K. Chu, and K. Huo, Carbon **197**, 238–245 (2022).
[45]G. Zhao, K. Rui, S. X. Dou, and W. Sun, Adv. Funct. Mater. **28**, 1803291 (2018).
[46]P. Xiong, X. Ao, J. Chen, J.-G. Li, L. Lv, Z. Li, M. Zondode, X. Xue, Y. Lan, and C. Wang, Electrochim. Acta **297**, 833–841 (2019).
[47]B. Hammer and J. K. Norskov, Nature **376**, 238–240 (1995).
[48]X. Wang, W. Zhou, Y. Wang, L. Gong, X. Liu, and X. Zhou, Nano Energy **109**, 108253 (2023).
[49]Y. Zhang, P. Guo, S. Guo, X. Xin, Y. Wang, W. Huang, M. Wang, B. Yang, A. Jorge Sobrido, and J. B. Ghasemi, Angew. Chem., Int. Ed. **61**, e202209703 (2022).
[50]B. Liu, H. Li, B. Cao, J. Jiang, R. Gao, and J. Zhang, Adv. Funct. Mater. **28**, 1801527 (2018).
[51]H. Sun, C.-W. Tung, Y. Qiu, W. Zhang, Q. Wang, Z. Li, J. Tang, H.-C. Chen, C. Wang, and H. M. Chen, J. Am. Chem. Soc. **144**, 1174–1186 (2021).

Supporting Information

In-plane Heterostructured MoN/Mo_2N Nanosheets as High-Efficiency Electrocatalysts for Alkaline Hydrogen Evolution Reaction

Xiuen Luo,[1,2,†] Hao Song,[1,4,†] Yulei Ren,[1] Xuming Zhang,[1] Kaifu Huo,[2,3,a)] Paul K. Chu[4]

[1] The State Key Laboratory of Refractories and Metallurgy, Institute of Advanced Materials and Nanotechnology, Wuhan University of Science and Technology, Wuhan 430081, China

[2] Wuhan National Laboratory for Optoelectronics (WNLO), Huazhong University of Science and Technology, Wuhan 430074, China

[3] Research Institute of Huazhong University of Science and Technology in Shenzhen, Shenzhen 518063, China

[4] Department of Physics, Department of Materials Science and Engineering, and Department of Biomedical Engineering, City University of Hong Kong, Tat Chee Avenue, Hong Kong, China

[†] These authors contributed equally.

[a)] **Authors to whom correspondence should be addressed:**
kfhuo@hust.edu.cn

Equations related to electrochemical measurements

The electric double-layer capacitance (C_{dl}) is calculated as follows:

$$\Delta j = \nu C_{dl}$$

where ν is the scan rate and Δj is half of the difference in current density of the CV curve ($\Delta j = (ja - jc)/2$).[1]

C_{dl} and electrochemically active surface area (ECSA) are linearly related. Therefore, ECSA can be calculated from C_{dl} by the following equation:

$$ECSA = C_{dl}/C_s$$

where C_s represents the specific capacitance per unit area of surface under certain conditions.[2]

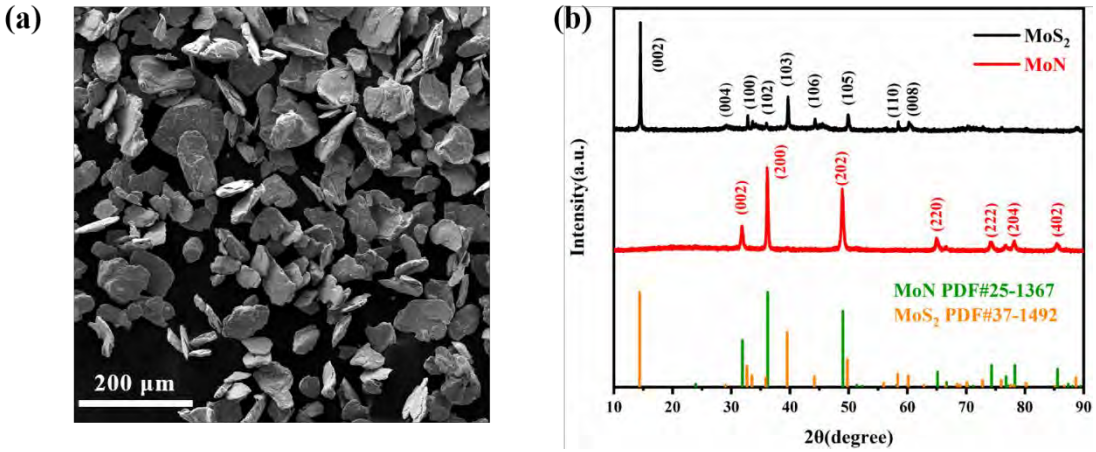

Fig. S1. (a) SEM images of MoS_2; (b) XRD patterns of MoS_2 and MoN.

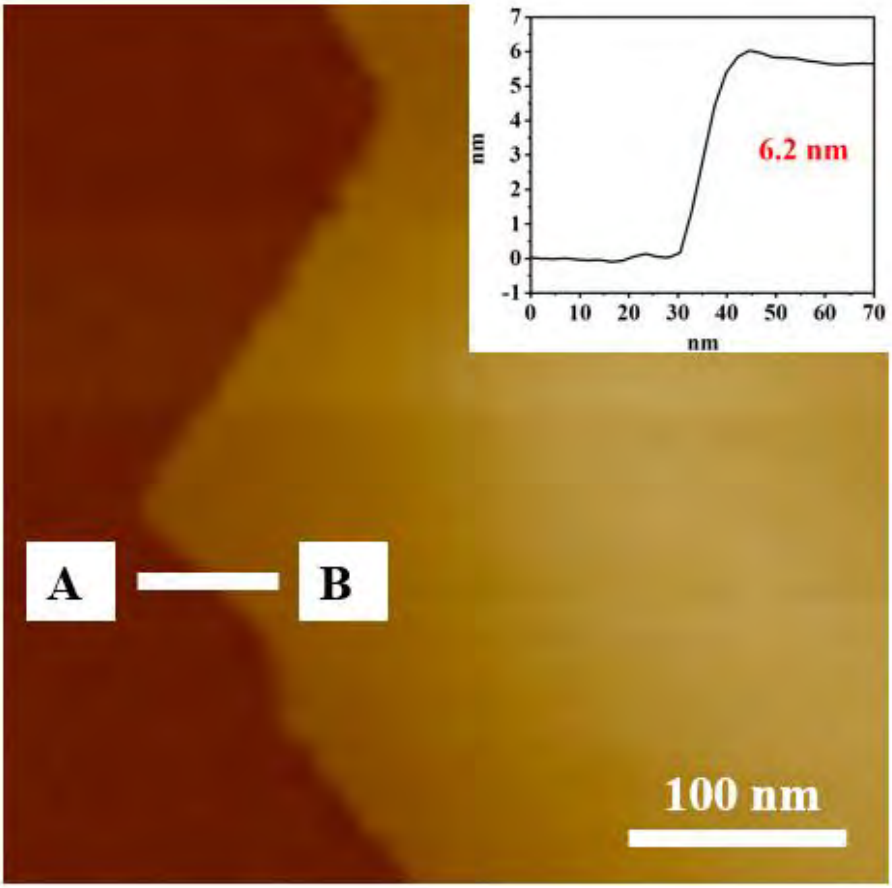

Fig. S2. AFM image of MoN.

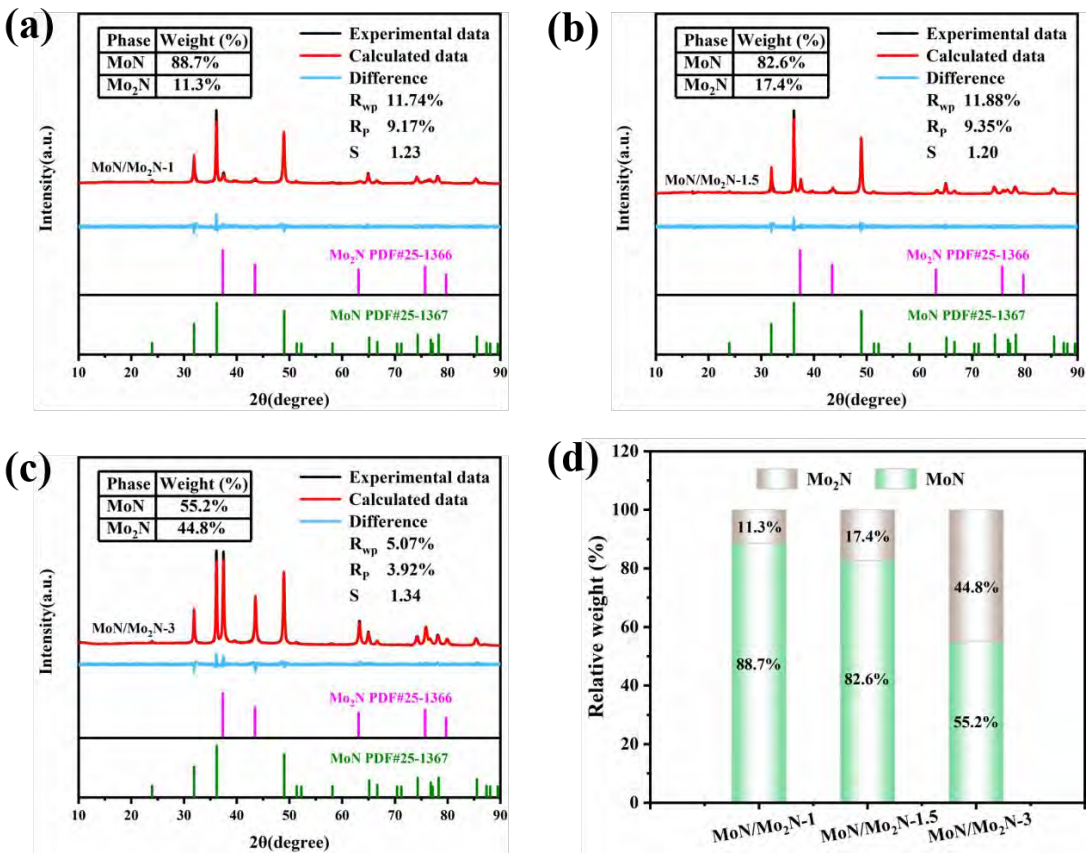

Fig. S3. Rietveld refinement analysis: (a) MoN/Mo_2N-1; (b) MoN/Mo_2N-1.5; and (c) MoN/Mo_2N-3; (d) Relative weights of MoN and Mo_2N by the Rietveld refinement analysis.

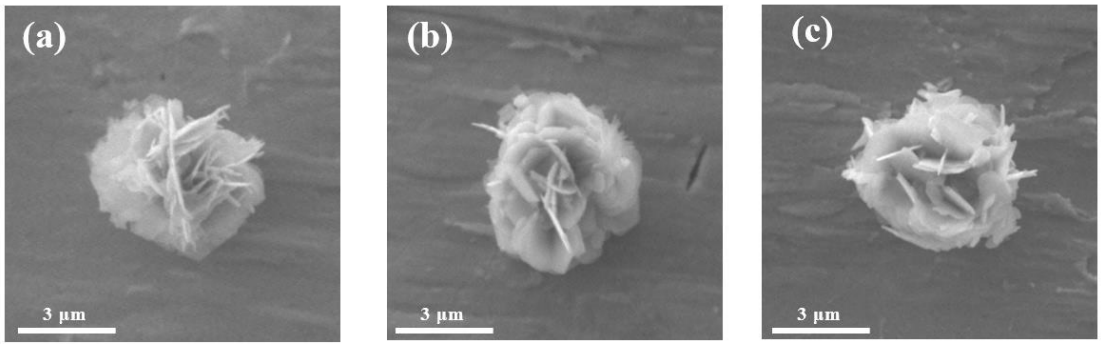

Fig. S4. SEM images of (a) MoN; (b) MoN/Mo_2N-1.5; (c) Mo_2N.

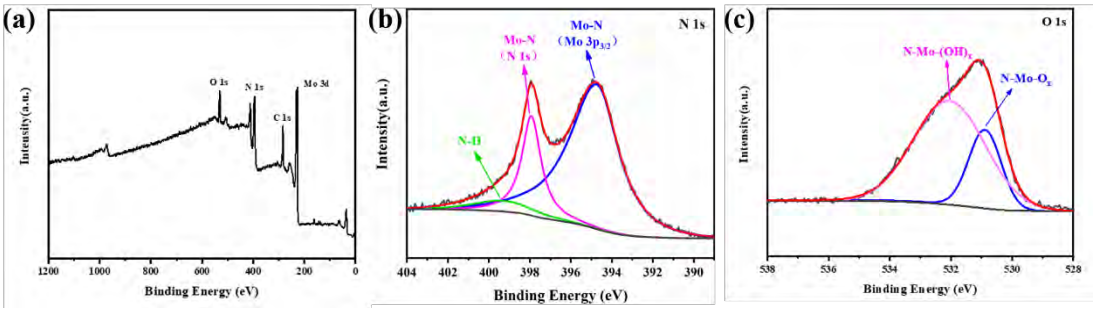

Fig. S5. (a) Survey XPS spectrum of MoN/Mo_2N-1.5; (b) XPS N 1s spectrum of MoN/Mo_2N-1.5; (c) XPS O 1s spectrum of MoN/Mo_2N-1.5.

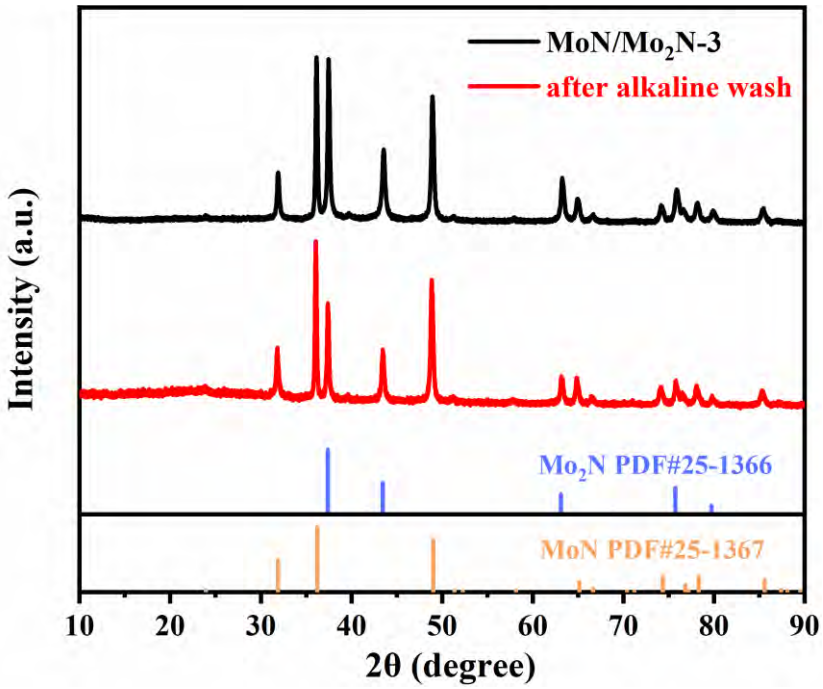

Fig. S6. XRD patterns of MoN/Mo_2N-3 before and after alkaline wash (6 M NaOH).

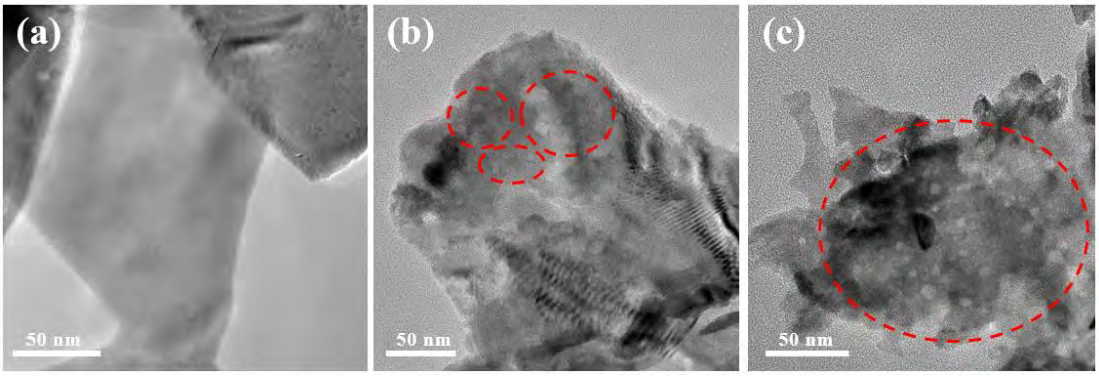

Fig. S7. TEM images of (a) MoN/Mo_2N-3; (b-c) MoN/Mo_2N-3 after alkaline wash (6 M NaOH).

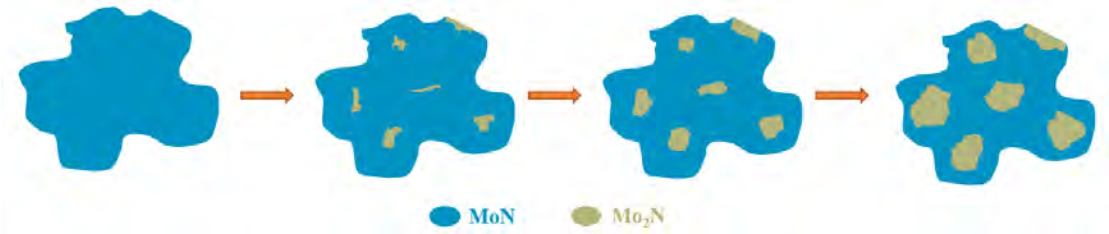

Fig. S8. Growth mechanism of MoN/Mo_2N heterojunctions.

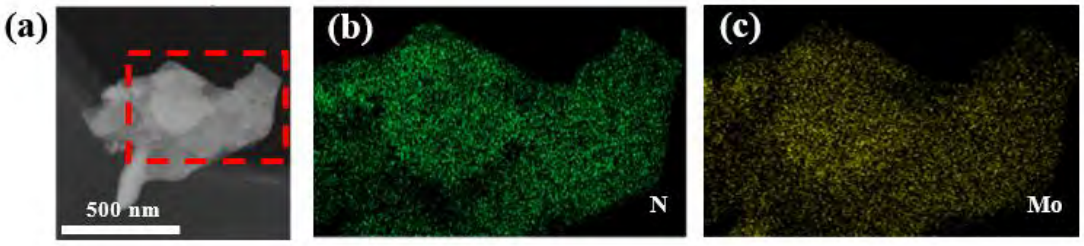

Fig. S9. (a-c) EDS elemental maps of MoN/Mo_2N-1.5.

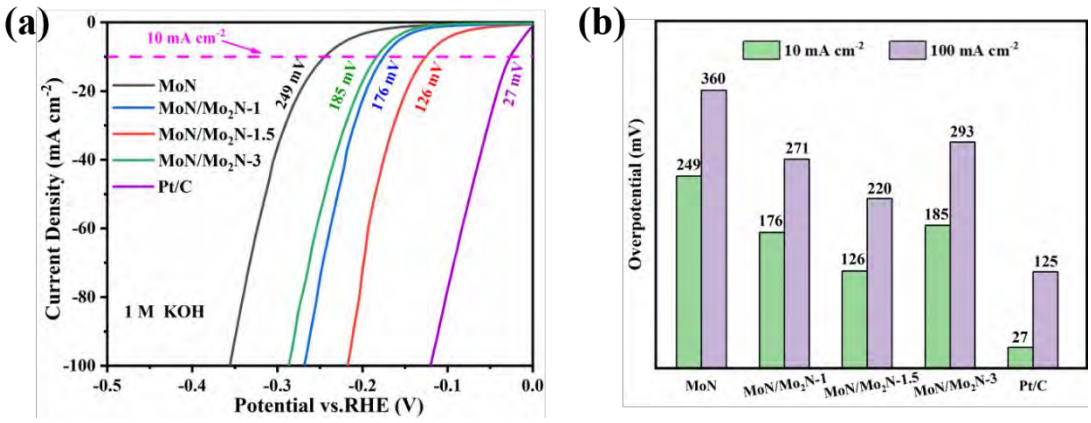

Fig. S10. HER activity in 1 M KOH. (a) Polarization curves (LSV) and Tafel slopes of MoN, MoN/Mo_2N-1, MoN/Mo_2N-1.5, and MoN/Mo_2N-3, Pt/C and (b) Histograms of the corresponding LSV curves for current densities of 10 and 100 mA cm^{-2}.

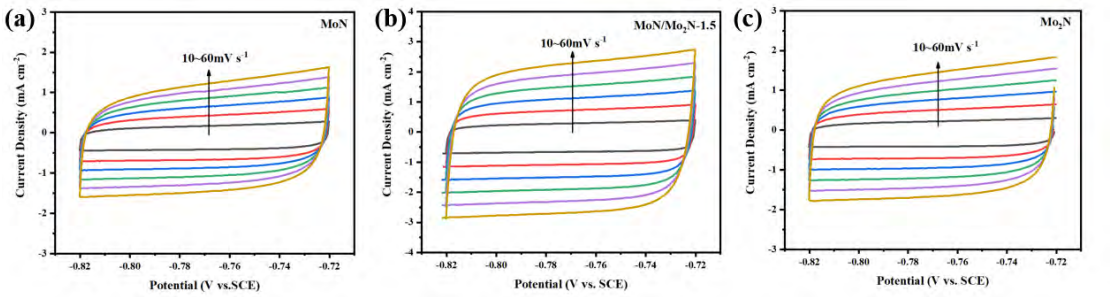

Fig. S11. Electrochemical capacitance measurements: (a) MoN; (b) MoN/Mo_2N-1.5; (c) Mo_2N.

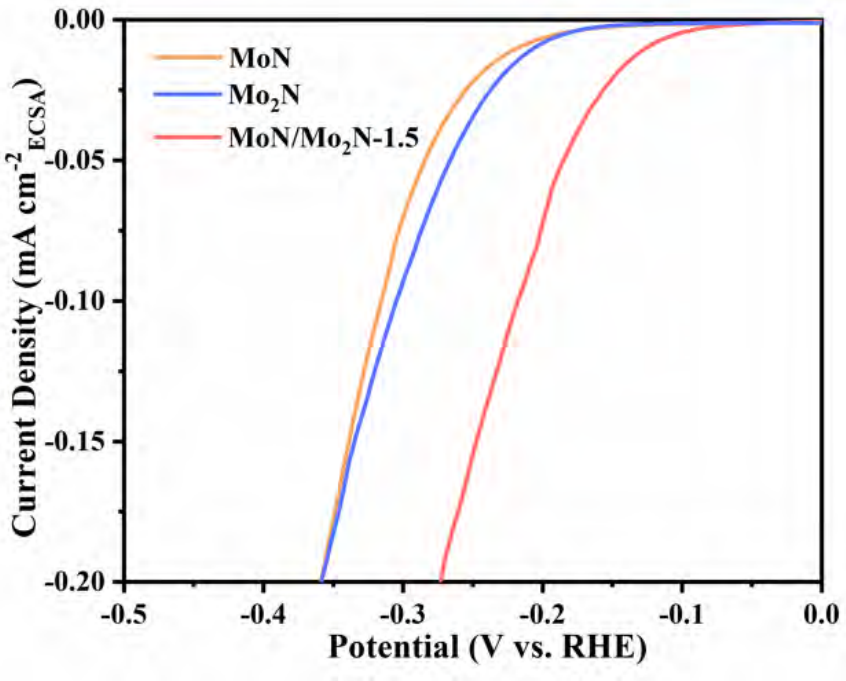

Fig. S12. Normalized HER polarization curves of MoN, Mo_2N and MoN/Mo_2N.

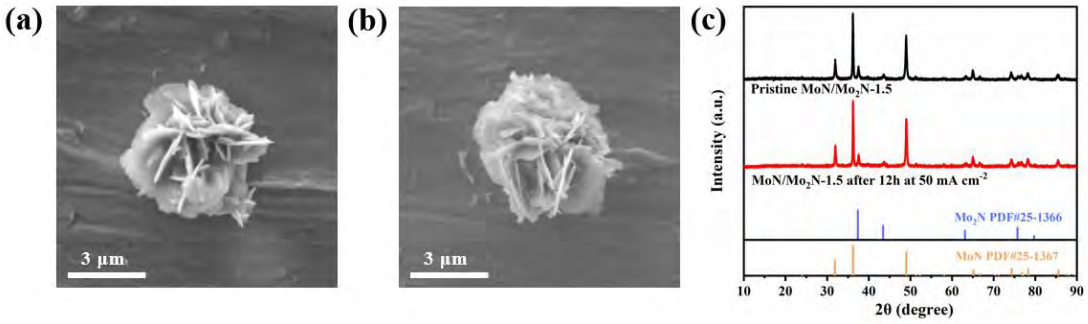

Fig. S13. (a) SEM images of MoN/Mo_2N-1.5; (b) SEM images of MoN/Mo_2N-1.5 after 12 h at a current density of 50 mA cm^{-2}; (c) XRD patterns of MoN/Mo_2N-1.5 before and after stability test.

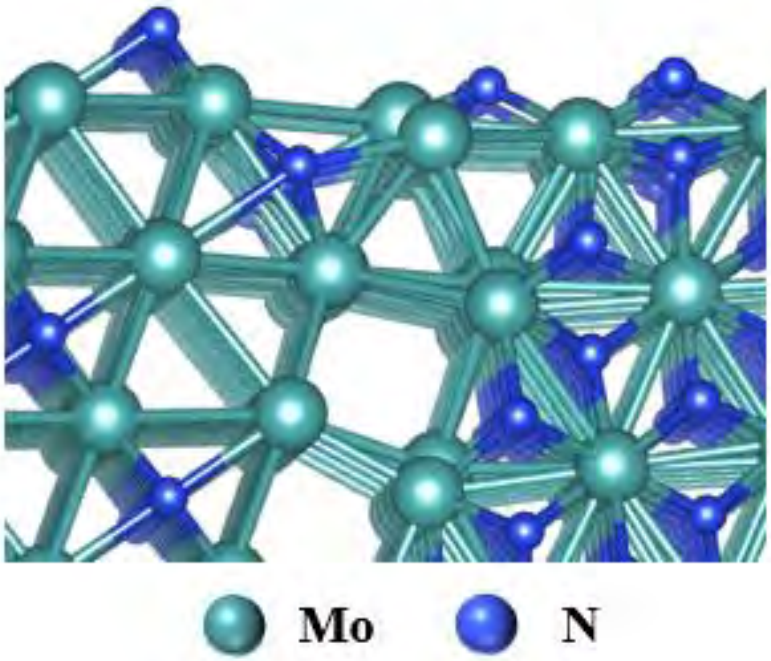

Fig. S14. Geometric structure of the MoN/Mo_2N heterojunction.

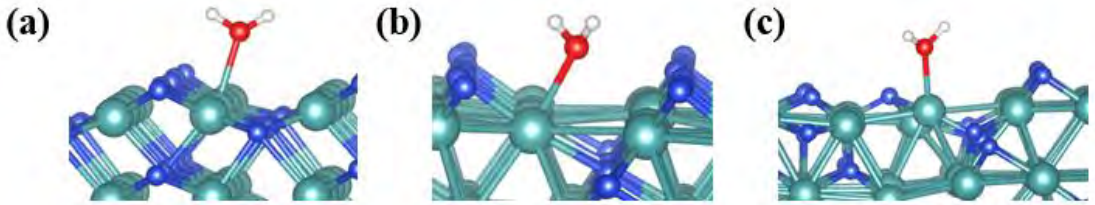

Fig. S15. Water adsorption on (a) (200) plane of MoN; (b) (111) plane of Mo_2N, and (c) MoN/Mo_2N interface.

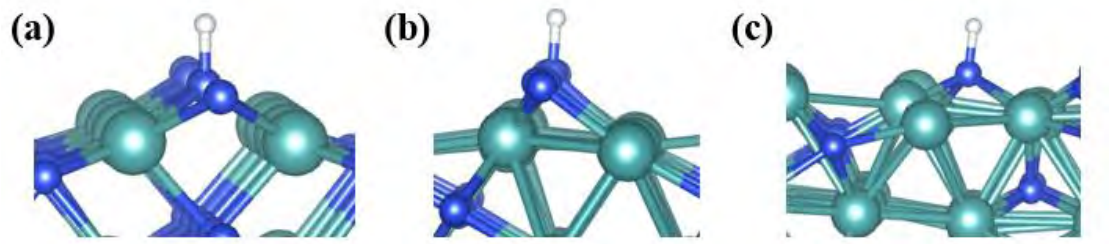

Fig. S16. Hydrogen adsorption free energy (ΔG_{H^*}) of (a) (200) plane of MoN; (b) (111) plane of Mo_2N, and (c) MoN/Mo_2N interface.

Table S1. Comparison in HER performance of molybdenum-based nitride catalysts in 1 M KOH

Electrocatalysts	η_{10} (mV)	Tafel slopes (mV dec^{-1})	Refs.
MoN/Mo_2N	126	69.5	in this work
MoS_2/MoN	132	98	3
MoO_2@MoN/NF	152	98	4
$NiMo_{0.75}N$@NC	164	103	5
Ni/MoN	207	93	6
Edge MoN	248	55	7
MoN/NC	141	65	8
D-MoP/Mo_2N	144	103	9
Mo_2C-MoN/Ni@NC	183	107	10
Mo_2C/N-C(S)	271	90	11

REFERENCES

[1] C. F. Yang, R. Zhao, H. Xiang, J. Wu, W. D. Zhong, W. L. Li, Q. Zhang, N. J. Yang and X. K. Li, Adv. Energy Mater. **10**, 2002260 (2020).

[2] Z. P. Shi, Y. X. Wang, H. L. Lin, H. B. Zhang, M. K. Shen, S. H. Xie, Y. H. Zhang, Q. S. Gao and Y. Tang, J. Mater. Chem. A. **4**, 6006-6013 (2016).

[3] A. P. Wu, Y. Gu, Y. Xie, H. J. Yan, Y. Q. Jiao, D. X. Wang and C. G. Tian, J. Alloy. Compd. **867**, 159066 (2021).

[4] Y. Sun, Y. L. Zhou, Y. P. Zhu, Y. H. Shen and A. J. Xie, ACS Sustainable Chem. Eng. **7**, 9153-9163 (2019).

[5] B. L. Jiang, Y. Y. Cui, S. S. Jie, N. Jiang and W. Q. Tan, Acta Chim. Sinica **80**, 1394 (2022).

[6] P. Wang, J. Qi, C. Li, X. Chen, T. H. Wang and C. H. Liang, ChemElectroChem **7**, 745-752 (2020).

[7] Y. Q. Wang, C. Y. Jian, W. T. Hong and W. Liu, Chem. Commun. **57**, 223-226 (2021).

[8] C. Huang, X. L. Zhang, J. Tang, D. Li, Q. D. Ruan, L. L. Liu, F. Y. Xiong, B. Wang, Y. Xu and S. H. Cui, Rare Metals, 1-7 (2023).

[9] Y. Gu, A. P. Wu, Y. Q. Jiao, H. R. Zheng, X. Q. Wang, Y. Xie, L. Wang, C. G. Tian and H. G. Fu, Angew. Chem. Int. Ed. **60**, 6673-6681 (2021).

[10] Y. F. Zhan, F. Y. Xie, H. Zhang, Z. P. Lin, J. L. Huang, W. H. Zhang, X. L. Sun, H. Meng, Y. L. Zhang and J. Chen, J. Electrochem. Soc. **165**, F75 (2018).

[11] M. Ji, S. Q. Niu, Y. C. Du, B. Song and P. Xu, ACS Sustainable Chem. Eng. **6**, 11922-11929 (2018).